

# On Hydrodynamic Diffusion and Velocity Fluctuations in Two-Dimensional Simulations of Sedimentation

**W. Kalthoff<sup>1</sup>, S. Schwarzer<sup>1</sup>, G.H. Ristow<sup>2</sup> and H. J. Herrmann<sup>3</sup>**

May 9, 2021

<sup>1</sup> HLRZ, c/o Forschungszentrum Jülich  
52425 Jülich, Germany

<sup>2</sup> Fachbereich Physik, Philipps-Universität Marburg  
35032 Marburg, Germany

<sup>3</sup> LPMMH, ESPCI, 10 rue Vauquelin  
75231 Paris Cedex 05, France

## Abstract

We present a numerical method to deal efficiently with large numbers of particles in incompressible fluids. The interactions between particles and fluid are taken into account by a physically motivated ansatz based on locally defined drag forces. We demonstrate the validity of our approach by performing numerical simulations of sedimenting non-Brownian spheres in two spatial dimensions and compare our results with experiments. Our method reproduces essential aspects of the experimental findings, in particular the strong anisotropy of the hydrodynamic bulk self-diffusivities.

# I Introduction

An important paradigm problem of multiphase flow, incorporating aspects of both a discrete particulate and a continuous liquid phase, is the sedimentation problem. Here the particulate phase slowly settles into a packed bed at the bottom of a container filled with viscous liquid. The main theoretical challenge in the sedimentation problem is the understanding of the long range liquid mediated hydrodynamic interactions between the immersed particles. Many aspects are well studied and understood, as are for example the mean sedimentation velocity  $\langle V \rangle$  in the Stokes flow regime for a monodisperse [1, 2, 3] or a polydisperse system [4]. Less well understood are fluctuation phenomena, for example the properties of the particle velocity distribution, as, e.g., its variance, time autocorrelation, and effects arising from particle polydispersity. Recently, much attention has been focused on the long time behavior of the particle motion as described by strongly anisotropic hydrodynamic diffusion constants [5]. Moreover, most analytical work pertains to the regime of dilute suspensions, whereas semi-dilute and concentrated suspensions still present a challenge to theoreticians.

The focus of this paper is the application of a novel computer simulation method for particulate multiphase flow [6] to the sedimentation problem. Among the standard computational approaches to multiphase flow in general and the sedimentation problem in particular are (i) continuum descriptions [7, 8] that neglect the discrete nature of the particulate phase, (ii) methods that exploit the linearity of the Navier-Stokes equations at very small Reynolds numbers for either the simulation of hydrodynamically interacting point Stokeslets [9, 10] or extended spheres [11, 12, 13], (iii) finite element and finite difference techniques in two (2D) or three dimensions (3D) that represent the proper Navier-Stokes equations with no-slip boundary conditions for the liquid on the particle surface, and (iv) algorithms that combine a continuum description for the liquid phase with a discrete representation of the particulate phase [14].

All of these approaches have inherent strengths and weaknesses. The continuum approaches (i) suffer from difficulties to represent the particulate phase in terms of continuum quantities as pressure and stress. Both the Stokes flow methods (ii) and the differencing schemes (iii) give very reliable results where they apply. However, the Stokes flow methods (i) are in principle restricted to low Reynolds number flow and inherent to the differencing schemes (iii) is a tremendous computational effort that limits their applicability to systems with very few particles [15]. We therefore choose a method of class (iv) comprising basically a Lagrangian integration of particle trajectories coupled by local drag-force terms to a Eulerian Navier-Stokes integration.

Such a method allows immediate access to basically all physically relevant quantities in the system, including particle coordinates and both particle and liquid velocities, at little more computational costs than a standard real space Navier-Stokes integration. The main drawback is that a neglect of the proper boundary conditions between particles and liquid will result in inaccurate rendering of the short scale flow properties. However, we will be mainly concerned with collective phenomena, i.e., the effects that arise when the number of particles is large and we do not have the ambition to describe accurately the local flow fields [15] on the scale of the particle size. Single particle and particle pair movement can to a high degree of accuracy be treated analytically [16].

Nevertheless we want to see which and how phenomena emerge directly from simple modeling assumptions — as opposed to using semi-empirical expressions as, e.g., done in Refs. [14, 10]. In particular, we rely on the fact that the long-range hydrodynamic interactions, which we presume to be the most important for collective phenomena, are

correctly represented by the velocity and pressure fields evolved by the Navier-Stokes integration.

In this paper, we will first describe a two-dimensional (2D) implementation of our simulation technique in Sec. II. We will then describe simulations of the sedimentation problem in a broad range of particle solid fractions. We first show particle trajectories resulting in the sedimenting bulk (Sec. III.A). As function of the solid fraction, we address and discuss the hydrodynamic diffusion (Sec. III.B), the hindered settling function (Sec. III.C) and particle velocity fluctuations (Sec. III.D).

## II Simulation Technique

### II.A Modeling assumptions

Our aim is to capture the large scale collective processes of the combined particle-liquid system with a computer simulation. Therefore we need to model comparatively large systems in moderate time. We aim at the development of a tool that allows simple checks of qualitative and quantitative behavior of multiphase flow. To this end we concentrate on the momentum exchange between particle and liquid phase. Our simulation technique makes physically motivated assumptions to simplify the computational difficulties associated with a full treatment of the no-slip boundary conditions. Our assumptions are as follows.

(i) For small Reynolds numbers lubrication forces dominate as particles approach each other or the walls of the container. These forces of dissipative nature theoretically prevent particles from touching each other. Since we are interested in long-range effects, we neglect the short-range lubrication forces, and use instead a simple contact model between particles.

In 2D, the particles  $i$  are represented by disks with radii  $r_i$  chosen from a Gaussian distribution  $h_p(r/\bar{r})$  with mean  $\bar{r}$ , which is cut off at its standard deviation  $\sigma$ ,

$$h_p(r/\bar{r}) \propto \begin{cases} \exp \left[ -\frac{1}{2} \frac{(r/\bar{r} - 1)^2}{p^2} \right], & \text{if } |r/\bar{r} - 1| < p, \\ 0, & \text{else.} \end{cases} \quad (1)$$

Here, the distribution is written in terms of the dimensionless radius  $r/\bar{r}$  and the polydispersity parameter  $p$ , which we define for the purposes of this paper to be the standard deviation of the original, full Gaussian divided by the mean radius, i.e.  $p \equiv \sigma/\bar{r}$ .

Our contact model assumes elastic, central, and repulsive forces, which act when two particles  $i$  and  $j$  touch each other [14, 17, 18, 19]. That is, the forces between two particles are zero unless the distance between their two centers is less than the sum of the radii  $r_i + r_j$ . Then the acting force is assumed to be

$$\vec{F}_{\text{el}} = -k_n(r_i + r_j - (\vec{x}_j - \vec{x}_i) \cdot \hat{n}_{ji}) \hat{n}_{ji}. \quad (2)$$

Here  $\vec{x}_i = (x_i, y_i)$  is the position vector of the center of particle  $i$  and  $\hat{n}_{ji}$  is the unit vector pointing from the center of particle  $i$  to the center of  $j$ . The spring constant  $k_n$  (cf. Table 1) describes the repulsion due to lubrication forces and depends on the size and shape of the colliding bodies. Tests including a velocity proportional damping term in Eq. (2) show that our simulation results do not significantly depend on the details of the particle-particle interactions.

Apart from the drag forces  $\vec{F}_d$ , which will be addressed below, we further add gravity (including buoyancy) as a contribution to the total force acting on each single particle,

$$\vec{F}_{\text{tot}} = \vec{F}_d + \vec{F}_{\text{el}} + \frac{4}{3}\pi r_i^3(\rho_p - \rho_l)\vec{g}. \quad (3)$$

Here,  $\rho_p$  and  $\rho_l$  are the densities of the particulate and the liquid phase respectively, and  $\vec{g}$  the earth's gravitational acceleration which is assumed to act in  $-y$  direction for the rest of this paper. Once we know all forces, we employ a fifth order Gear predictor-corrector integration algorithm to obtain the particle trajectories [20]. Rotational degrees of freedom are not considered.

(ii) We will assume that the exact arrangement of particles and the exact distribution of the interstitial liquid on short scales do not affect the qualitative features of the large-scale flow pattern. As already mentioned above this means we neglect detailed lubrication forces resulting from the no-slip boundary conditions of the stress tensor at the liquid-particle interfaces, replacing them by the above described particle interactions. For particle Reynolds numbers  $Re = \bar{r}\rho_l|\vec{V}_i - \vec{v}_i|/\eta$  smaller than one, we propose to model the momentum exchange between single particles and the surrounding liquid by means of a Stokes-type drag force,

$$F_d = C_d \eta r_i (\vec{V}_i - \vec{v}_i), \quad (4)$$

here  $\vec{v}_i$  denotes the velocity of particle  $i$ ,  $\vec{V}_i$  is an average *local* liquid velocity at the position of the particle and  $\eta$  denotes the liquid's kinematic shear viscosity. Equation (4) with  $C_d = 6\pi$  holds exactly in three dimensions (3D) for a single sphere moving with respect to the liquid resting at infinity. We obtain the  $V_i$  by linear interpolation of the liquid velocities from the four grid points of the quadrilateral MAC [21] mesh of the liquid integration surrounding the particle center.

In our case,  $C_d$  is a parameter. For all choices of grid and particle size we determine  $C_d$  such as to obtain the Stokes velocity for the simulation of a single sphere falling in a viscous liquid. Commonly<sup>1</sup>, we use grids sufficiently large so that  $C_d$  does not differ from  $6\pi$  by more than a factor of 2. The main physical effect of this local drag force is to introduce a tendency to locally equalize the liquid and particle velocities, similar to the no-slip boundary condition that implies particle and liquid velocities being equal on the particle surface.

## II.B Fluid Model

To describe the time evolution of the velocity and pressure fields  $\vec{v}$  and  $p$  of the fluid in our simulations we start with the Navier-Stokes equations,

$$\rho_l \left[ \frac{\partial \vec{v}}{\partial t} + (\vec{v} \cdot \nabla) \vec{v} \right] = -\nabla p + \eta \nabla^2 \vec{v} + \vec{f}. \quad (5)$$

Here,  $\rho_l$  denotes the liquid density and  $\eta$  its shear viscosity,  $\vec{f}$  is the volume force density in the system, including gravity, drag-force density and buoyancy response. Since we have in mind applications to liquid systems or gaseous systems with typical velocities much smaller than the velocity of sound, we complement these equations by the incompressibility constraint,

$$\nabla \cdot \vec{v} = 0. \quad (6)$$

---

<sup>1</sup> We find that the “drag coefficient”  $C_d$  depends on the dimensionless ratio of particle radius to grid spacing (see Sec. II.B),  $r/\Delta x$ . In the regime of particle Reynolds numbers  $Re \approx 0.5$  for our simulations we have determined the empirical relationship  $C_d/6\pi = 1 + 6.27(\Delta x/r)^{-1.5}$ .

Equation (6) presents a constraint on the velocity field that must be fulfilled at all times and may be employed to obtain the pressure field via an iterative procedure [22]. We will sketch the basic ideas briefly and refer the reader for more details to Refs. [21], [22] and [23].

The pressure as well as the velocity components  $v_x$  and  $v_y$  are located on three quadrilateral meshes with lattice spacing  $\Delta x$ . With respect to the pressure grid, the grids for the  $x$  and  $y$  velocity components are shifted by  $\Delta x/2$  in  $x$  and  $y$  direction respectively — this construction is commonly referred to as the MAC mesh and has several computational advantages, i.e., it is a simple means to avoid numerical instabilities due to mesh decoupling [21].

We obtain the pressure and the velocity components by an iterative procedure. Let the index  $n$  refer to values at time  $t = t_n$  and  $n + 1$  to those at  $t = t_{n+1} = t_n + \Delta t$  after a timestep of duration  $\Delta t$ . The index  $k$  shall denote an iteration index. We define  $p_{n+1,0} \equiv p_n$ , i.e., we start an iteration for the new pressure at time  $t_{n+1}$  with the old values at  $t_n$ . We obtain a tentative velocity field at  $t = t_{n+1}$  from an evaluation of the discretized Navier-Stokes equation,

$$\rho_1 \frac{\vec{v}_{n+1,k+1} - \vec{v}_n}{\Delta t} = -\rho_1(\nabla \vec{v}_n) \vec{v}_n - \nabla p_{n+1,k} + \vec{f}_n + \eta \nabla^2 \vec{v}_n. \quad (7)$$

A von Neumann stability analysis [21, 23] of the described discretization of the Navier-Stokes equation shows that the values  $\Delta x$  and  $\Delta t$  are subject to the two stability constraints

$$\Delta t \leq \frac{4\eta}{\rho_1(|v_x^{\max}| + |v_y^{\max}|)^2}, \quad (8)$$

and

$$\Delta t \leq \frac{\rho_1(\Delta x)^2}{4\eta}. \quad (9)$$

In general, the velocity field  $\vec{v}_{n+1,k+1}$  resulting in (7) does not satisfy the incompressibility constraint (6). To the end of lowering the modulus of the divergence of the velocity field — in so far it differs from zero — we calculate a new, likewise tentative, pressure field

$$p_{n+1,k+1} = p_{n+1,k} - \lambda \rho_1 \nabla \vec{v}_{n+1,k+1}. \quad (10)$$

Here, a large value of the parameter  $\lambda$  is crucial for rapid convergence. It is, however, by stability requirements constrained to

$$0 \leq \lambda \leq \frac{(\Delta x)^2}{4\Delta t}. \quad (11)$$

Subsequently new velocity values consistent with the  $p_{n+1,k+1}$  may be obtained using Eq. (7), or equivalently, without reevaluation of the Navier-Stokes equation, using the relation

$$\rho_1 \frac{\vec{v}_{n+1,k+2} - \vec{v}_{n+1,k+1}}{\Delta t} = \nabla(p_{n+1,k+1} - p_{n+1,k}). \quad (12)$$

Iterating Eqs. (10) and (12) yields a new pressure field and after convergence a consistent, divergence free velocity field for time  $t_{n+1}$ . This iteration is equivalent to solving a Poisson equation for the pressure.

For our purposes, the described algorithm has three advantages. It (i) generalizes straightforwardly to 3D and (ii) unlike spectral or streamfunction methods it gives immediate access to the quantities  $p$  and  $\vec{v}$  in real space. Fast access to the latter is crucial

for the drag-force calculation in Eq. (4). Moreover (iii), only the chosen coarseness of the spatial and temporal discretization limits the range of Reynolds numbers addressable in the simulation. The use of multi-grid techniques instead of the above local iterative method will improve the speed of our method for large system sizes.

For the present paper we have implemented the above set of equations in 2D. The uncoupled liquid and particle equations of motion are directly obtained by dropping the third  $z$ -component of the velocity and applying 2D versions of the differential operators to the liquid equations. The coupling of the two sets of equations, however, presents some problems. A 2D simulation should, strictly speaking, be one of rigid, parallel cylinders moving in a liquid that only displays motion in the  $xy$  plane. However, at a fixed small Reynolds number, the drag per unit length of a cylinder [24] does not depend on its radius in an infinitely large system. Thus, qualitative effects of particle polydispersity cannot be expected to be present in such a model. We therefore chose to refer the Stokes drag Eq. (4) to a reference length  $z$  equal to the average particle diameter. Alternatively, one may think of  $z$  as the depth of the liquid filled vessel, in which 3D spheres move such that their motion is constrained to lie in the  $xy$  plane. The Stokes drag per length then enters the particle and liquid equations as coupling term. Since we have not included any Brownian motion of the particles our model is only applicable in the non-Brownian regime of large Péclet numbers  $Pe \gg 1$ , characterized by comparatively large particles and low temperatures (cf. Sec. III.D).

All our simulations are performed in a rectangular vessel of width  $L_x$  and height  $L_y$ . On the walls of the container we impose no-slip boundary conditions, i.e., the liquid velocity there is taken to be zero. The particles are initially placed randomly and without overlap within the vessel. Their size is characterized by their mean radius  $\bar{r}$  and the degree  $p$  of polydispersity, which is kept constant and equal to 0.04 in all the simulations presented in this paper. See table 1 for a detailed list of simulation parameters.<sup>2</sup>

In the simulation the particles are point like and their volume only comes into play via the drag force. Presently, the model does not take into account the fractions of solid and liquid in a given volume element. This fraction, which is very important to describe backflow, will be included in a more extensive study [6].

### III Results and Discussion

In the remainder of this paper, we wish to show that the set of equations above — even if they might appear to be rather crude — constitute a reasonable description of a particulate two-phase system, and are, in particular, capable of reproducing the essential aspects of a sedimentation process.

#### III.A Particle trajectories in batch settling

We first consider the particle trajectories in a batch settling experiment. Typical experiments [5, 25] examine the behavior of a mixture of glass beads in a liquid kept in a container. The glass beads start to sink leaving behind clear liquid at the top and particle layers on the bottom of the vessel. Index matching techniques allow to trace the trajectories of single particles in the mixture [5]. In the limit of infinite dilution, in

---

<sup>2</sup> A typical simulation run is characterized by about 3 200 nodes for the liquid integration and about 1 500 particles. It involves about  $10^4$  full timesteps for the liquid and  $10^6$  timesteps for the particle integration. On a SPARC 20 workstation the required CPU time is of the order of 10h.

sufficiently large vessels these trajectories are straight lines from the top to the bottom of the container. The particle velocity is the Stokes velocity  $V_S(r_i) = (2/9)gr_i^2(\rho_p - \rho_l)/\eta$ , the terminal velocity of a sphere of radius  $r_i$  settling in an extended viscous liquid under the influence of gravity. For the purposes of this paper we will neglect the influence of polydispersity and set  $V_S \equiv V_S(\bar{r})$ .

At finite concentrations, particles start to feel each others presence and the trajectories are no longer straight. One observes very complicated collective effects of the suspension which organizes into continuously changing regions in which particles move in different directions. Denser regions with more particles per unit volume drag liquid with them and the displaced fluid travels upward through less dense regions that present less resistance to the flow. On smaller scales particle velocities change due to close encounters. The resulting typical particle trajectories are highly irregular. Even in the laboratory frame, one finds particles moving upward in the suspension, describing loops and displaying settling tendencies only if observed for long enough time.

For illustration we show in Fig. 1a the trajectories of 20 *randomly* selected particles out of a 1000 settling in a suspension at solid volume fraction  $\Phi = 0.157$ . Here, the solid fraction is the dimensionless ratio of the area in the  $xy$ -plane covered by disks to the total area in the simulation, i.e.,

$$\Phi \equiv \sum_i \pi r_i^2 / L_x L_y. \quad (13)$$

In Fig. 1b we display the same trajectories as viewed from the comoving frame, i.e., we subtract the mean settling velocity from the particle velocities in the lab frame and shift the trajectories such that they all start in one point. For long enough times each trajectory displays the characteristics of a random walk. Its direction changes frequently on scales larger than a coherence length, which measures the average distance that a particle has to travel before its motion becomes independent of the initial velocity.

In fact, experiments find that the particle velocities at large times decorrelate [5]. However, the motion is *anisotropic*, spreading much more rapidly in the main settling direction than perpendicular to it.

### III.B Diffusion constants

One may describe the long time behavior of the particle displacements in a sufficiently large system as a diffusion process in the frame comoving with the settling particles. The diffusion is characterized by its mean square displacements in vertical  $y$  and horizontal  $x$  direction,

$$\langle x^2(t) \rangle \equiv \frac{1}{N} \sum_i [x_i(t) - x_i(0)]^2, \quad (14)$$

$$\langle y^2(t) \rangle \equiv \frac{1}{N} \sum_i [y_i(t) - (y_i(0) + \langle V \rangle t)]^2. \quad (15)$$

The sum runs over those particles that are above the final bed height for  $t \rightarrow \infty$  at the given moment  $t$ . From their initial positions we determine the average motion to obtain  $\langle V \rangle$ .

As already indicated by Fig. 1b, a prominent feature of hydrodynamic diffusion in batch sedimentation is the strong anisotropy of the process with different diffusion constants  $D_x$  and  $D_y$  in horizontal and in vertical direction. Both  $D_x$  and  $D_y$  are obtained

from the long time behavior of the particle displacement by the relations

$$\langle x^2(t) \rangle \simeq 2D_x t, \quad (16)$$

$$\langle y^2(t) \rangle \simeq 2D_y t. \quad (17)$$

In practice, the squared particle displacements saturate due to the finite system size after passing a regime linear in time. In this regime, one can determine  $D_x$  and  $D_y$  using Eqs. (16 and 17). We show typical example for the time dependence of the mean square displacements in Fig. 2. We have normalized both  $x$  and  $y$ -displacements by division through the squared particle radius, i.e.,  $\langle x_*^2 \rangle \equiv \langle x^2(t) \rangle / \bar{r}^2$  and accordingly  $\langle y_*^2 \rangle \equiv \langle y^2(t) \rangle / \bar{r}^2$ . We obtain the dimensionless time  $t^*$  by division of  $t$  through  $\bar{r}/V_S$ . The straight lines superposed to the data shall emphasize the approximately linear behavior for intermediate  $t^*$ . The slopes of these lines, averaged over several runs with different initial particle positions, are equal to twice the dimensionless diffusion constants  $D_x^*$  and  $D_y^*$  which result from division of  $D_x$  and  $D_y$  by the quantity  $\bar{r}V_S$ .

In Fig. 3a we plot  $D_x^*$  and  $D_y^*$  vs. the solid fraction  $\Phi$ . As is observed in real 3D experiments, also here the diffusion constants increase for small  $\Phi$  until in the simulations a maximum at area fraction  $\Phi \approx 0.12$  is reached. The location of the maximum in the experiments is at volume fraction  $\Phi \approx 0.1$  at a slightly lower value. At increasingly higher  $\Phi$  one observes a renewed decrease of the diffusion constants. The values of our 2D diffusion constants lie by a factor of  $\approx 2.5 \dots 3$  above the 3D experimental values [5] or 3D simulation results using Stokesian dynamics methods [12, 13].

Qualitatively, we understand the existence of a maximum at intermediate volume fractions. For  $\Phi \rightarrow 0$ , hydrodynamic interactions between the particles are not very pronounced and the  $D^*$  tend to small values. When  $\Phi$  increases, so does the importance of hydrodynamic interactions between particles and the increasing complexity of particle trajectories is reflected in an increasing diffusion constant. When  $\Phi$  increases further, then the importance of close particle encounters also increases, restricting the motion and consequently reducing the diffusion constants.

The degree of anisotropy of the diffusion is measured by the ratio  $D_y/D_x$ , which is equal to one in the isotropic case. In the experiments of Nicolai et al. [5] this ratio takes values around  $5 \dots 6$  up to  $\Phi \approx 0.20$ . For higher solid fractions the ratio decreases. Such a behavior may be expected when the importance of particle encounters increases which tends to drive the diffusion towards isotropy. As shown in Fig. 3b we observe a ratio  $D_y/D_x$  of about  $4 \dots 5$  at small  $\Phi$  decreasing to  $\approx 2 \dots 3$  at large  $\Phi$ .

### III.C Hindered settling function

One of the most easily accessible quantities in a batch settling experiment is the mean sedimentation velocity  $\langle V \rangle$ . It may be obtained by observation of the stable upper sedimentation front<sup>3</sup>, i.e., the interface between batch suspension and clear liquid, or as average of the velocity of the bulk particles, if the particles trajectories are traced individually as during an index matched settling experiment. The mean sedimentation velocity decreases as the solid volume fraction  $\Phi$  increases. For  $\Phi \rightarrow 0$  one obtains  $\langle V \rangle = V_S$ .

The ratio of sedimentation velocity  $\langle V \rangle$  to Stokes velocity is a dimensionless quantity, known as the hindered settling function  $f(\Phi)$ ,

$$f(\Phi) \equiv \langle V \rangle / V_S. \quad (18)$$

---

<sup>3</sup> In [26] an initially step-shaped concentration profile is reported to broaden due to hydrodynamic diffusion until a stationary smooth profile is reached after  $t^* \approx 400$ .



The hindered settling function is always smaller than one, decreases with solid volume fraction and is in most low Reynolds number [ $Re = \rho_l V_{sr}/\eta \ll 1$ ] experiments in 3D well described by the phenomenological Richardson-Zaki law [3],

$$f(\Phi) = (1 - \Phi)^n, \quad (19)$$

where  $n$  typically takes values around 5 in experiments. Theoretical considerations by Batchelor et al. [27] lead to

$$f(\Phi) = 1 - 5.6\Phi \quad (20)$$

for  $\Phi \rightarrow 0$  and  $Pe \gg 1$ . Mills et al. [2] use mean field and scaling arguments to arrive at the expression

$$f(\Phi) = (1 - \Phi)/[1 + k\Phi/(1 - \Phi)^3], \quad (21)$$

where  $k = 4.6$  in the non-Brownian regime is a parameter chosen to match Batchelor's result (20). Thus, these expressions all agree in the low concentration regime and are very well established experimentally [28]. Moreover, Eqs. (19) and (21) are accurate also at intermediate and high concentrations, not too close to the random packing threshold.

We display our simulation results in Fig. 4a where  $f(\Phi)$  is plotted vs. the effective 3D volume fraction  $\Phi$  of the simulation. Clearly,  $\langle V \rangle$  decreases when the solid volume fraction  $\Phi$  increases. However, the decrease is not as sharp as expected from the Richardson-Zaki law (19) or from Eq. (21). Our 2D simulation results are rather fitted approximately by  $f(\Phi) \approx (1 - \Phi)^3$  for small  $\Phi$ . This function is also plotted in Fig. 4a for comparison.

Apart from the fact that our simulations were done in 2D in contrast to the 3D experiments, two factors should lead to a sedimentation velocity that is too high compared to the experiments. (i) There is no provision in the simulation to take the volume of liquid into account that is displaced by the particles. Thus, our simulation does not fully reproduce the net upward backflow effect that otherwise counteracts the settling. However, some backflow effect is retained, because the frictional coupling between liquid and particles effectively attaches some liquid to every particle. When the particles settle, this liquid replaces the fluid present in the lower part of the container and a backflow results [9]. (ii) The lattice spacing sets the scale on which we resolve details of the flow. Particles act on the liquid by point-like drag forces located on the four grid points closest to the particle center. The coarser the grid, the less accurate is this model for the momentum transfer onto the liquid phase and we underestimate frictional drag because we underestimate the interstitial liquid velocities.

In fact, reducing the grid spacing leads to a more realistic representation of the interstitial particle velocities and as a consequence to smaller sedimentation velocities. We address this question more systematically in Fig. 4b, where we plot the simulated values of  $f(\Phi)$ , for several values of  $\Phi = 0.079, 0.16, 0.24, 0.31, 0.39$  vs. the ratio  $\Delta x/\bar{r}$ . In accord with the argumentation above, the simulated sedimentation velocity slightly decreases for most values as the grid becomes finer and resolves more details of the interstitial flow field.

### III.D Velocity fluctuations

Another interesting quantity is the distribution of velocities of the sedimenting particles. In particular, the standard deviation  $\Delta v_y$  of the  $y$ -velocity distribution has been measured by Xue et al. [25] and Nicolai et al. [5] in different experiments. Here we first focus on the dependence of the velocity fluctuations on volume fraction at fixed polydispersity  $p = 0.04$ , corresponding roughly to the particle size dispersion in the experiment by Nicolai et al.

To calculate the velocity variance  $\Delta v_y$ , in the simulation, we calculate in intervals of about  $\Delta t^* = 1$  the standard deviation of the instantaneous  $y$ -velocity distribution of selected particles. The selection of particles occurs according to the same rules as used for the determination of diffusion constants (cf. Sec. III.B). Then we time average the standard deviations for times  $t^* > 20$ , which we found sufficient to avoid significant influence from the initial transient behavior.

We then normalize  $\Delta v_y$  by division with  $V_S$  to obtain the dimensionless quantity  $\Delta v_y^*$ . Figure 5a shows  $\Delta v_y^*$  as a function of solid fraction  $\Phi$ . For comparison, we have added the measured values of Refs. [5, 25] into the plot. The two experimental data sets agree at large solid fractions, where they show a pronounced decrease of the fluctuations. At small solid fractions, the data from [5] passes through a maximum, whereas the data of [25] starts at so high  $\Phi$  that no such maximum is visible. Just as the experimental data, also the simulation data shows a decreasing branch for large solid fractions and displays a maximum of the fluctuations at intermediate solid fractions, as visible in one of the experimental data sets.

We explain the existence of a maximum in the velocity fluctuations by similar factors as have been invoked in the case of the hydrodynamic diffusion constants, which also pass through a maximum as functions of  $\Phi$ . For increasing volume fraction the fluctuations first increase due to the more important role of hydrodynamic interactions. For larger volume fractions, however, the fluctuations are reduced due to the increasing role of particle encounters, which are dissipative in nature and tend to reduce fluctuations.

In Fig. 5b we plot the ratio  $\Delta v_y^*/\Delta v_x^*$ . For large solid fractions our results match well the experimental data of Nicolai et al., but do not display the expected pronounced maximum for lower volume fractions which is visible in the experimental data. This could be due to the small system size limiting the fluctuations [29] and thereby flattening the  $\Delta v_y^*$  curve at intermediate solid fractions.

## IV Conclusions and Outlook

We have presented a comparatively simple and fast simulation method to calculate properties of particle suspensions. Although our simulations have been performed in 2D and involve a set of assumptions that may be considered to be rather crude, namely the exclusive consideration of translational degrees of freedom and a simplified local frictional coupling of the particulate and liquid phase, we have captured the essential features of 3D sedimentation experiments, like the solid fraction dependence of (i) the particle self-diffusion constants, (ii) the velocity fluctuations and (iii) the hindered settling function. Two advantages of our method are that it is (i) not a priori limited to 2D or (ii) to small Reynolds numbers. Moreover, more sophistication may enter the drag expression in order to improve the quantitative agreement with experiments once the program has been extended to 3D. We are currently working on the extension of the method both to 3D and to Reynolds numbers around 100.

## Acknowledgments

We are grateful for lively and helpful discussions with F. Feuillebois, J. Gallas, E. Guazzelli, J. Hinch, J. Hofhaus, L. Kjeldgaard, H.-G. Mattutis, S. Melin, C. Moukarzel, T. Pöschel, H.-J. Tillemans, W. Vermöhlen, and M. Weimer and with several participants of the NATO ASI “Mobile Particulate Systems.” GR thanks the statistical physics group at the

University of Marburg for fruitful discussions and comments. We are particularly grateful to M. Rutgers [25] and H. Nicolai [5] who supplied experimental data for comparison.

The numerical computations have been performed on workstations at the HLRZ, on the 144-node Intel XP/S 10 Paragon and the SP1 at the ZAM, Forschungszentrum Jülich and on the SP1 of the Gesellschaft für Mathematik und Datenverarbeitung in Bonn.

## References

- [1] G. K. Batchelor, "Sedimentation in a Dilute Dispersion of Spheres," *J. Fluid Mech* **52**, 245 (1972).
- [2] P. Mills and P. Snabre, "Settling of a Suspension of Hard Spheres," *Europhys. Lett.* **25**, 651 (1994).
- [3] J. F. Richardson and W. N. Zaki, "Sedimentation and Fluidisation: Part I," *Trans. Instn. Chem. Engrs.* **32**, 35 (1954).
- [4] R. H. Davis and H. Gecol, "Hindered Settling Function with No Empirical Parameters for Polydisperse Suspensions," *AIChE J.* **40**, 570 (1994).
- [5] H. Nicolai, B. Herzhaft, E. J. Hinch, L. Oger and E. Guazzelli, "Particle Velocity Fluctuations and Hydrodynamic Selfdiffusion of Sedimenting Non-Brownian Spheres," *Phys. Fluids*, to appear Jan. 1994.
- [6] S. Schwarzer and H. Herrmann, in preparation.
- [7] R. Jackson, "Hydrodynamic Stability of Fluid-Particle Systems," in *Fluidization* (J.F. Davidson, R. Clift and D. Harrison, eds.), pp. 47 (Academic Press, London, 1985).
- [8] S. L. Soo, *Fluid Dynamics of Multiphase Systems* (Blaisdell Publishing Co., 1967).
- [9] F. R. Da Cunha, contributed talk at NATO ASI "Mobile Particulate Systems," Cargese, 1994; J. Hinch, private communication.
- [10] K. Ichiki and H. Hayakawa, "Simulation of Granular Particles in Flow by the Stokesian Dynamics Method," *Int. J. Mod. Phys. B* **7**, 1899 (1993).
- [11] J. F. Brady and G. Bossis, "Stokesian Dynamics," *Ann. Rev. Fluid Mech.* **20**, 111 (1988).
- [12] A. J. C. Ladd, "Hydrodynamic Interactions in a Suspension of Spherical Particles," *J. Chem. Phys.* **88**, 5051 (1988).
- [13] A. J. C. Ladd, "Dynamical Simulations of Sedimenting Spheres," *Phys. Fluid A* **5**, 299 (1993).
- [14] Y. Tsuji, T. Kawaguchi and T. Tanaka, "Discrete Particle Simulation of Two-Dimensional Fluidized Bed", *Powder Technol.* **77**, 79 (1993).
- [15] J. Feng, H. H. Hu and D. D. Joseph, "Direct Simulation of Initial Value Problems for the Motion of Solid Bodies in a Newtonian Fluid Part 1. Sedimentation," *J. Fluid Mech.* **261**, 95 (1994).

- [16] J. Happel and H. Brenner, *Low Reynolds Number Hydrodynamics* (Prentice-Hall, Englewood Cliffs, 1965).
- [17] P. A. Cundall and O. D. L. Strack, *Géotechnique* **29**, 47 (1979).
- [18] G. H. Ristow, “Simulating Granular Flow with Molecular Dynamics,” *J. Phys. I France* **2**, 649 (1992); *Int. J. Mod. Phys. C* **3**, 1281 (1992); G.H. Ristow and H. J. Herrmann, “Density Patterns in Two-Dimensional Hoppers,” *Phys. Rev. E* **50**, R5 (1994).
- [19] O. R. Walton and R. L. Braun, *J. Rheol.* **30**, 949 (1986).
- [20] M. P. Allen and D. J. Tildesley, *Computer Simulations of Liquids* (Clarendon Press, Oxford, 1987).
- [21] R. Peyret and T. D. Taylor, *Computational Methods for Fluid Flow* (Springer-Verlag, New York, 1983).
- [22] A.J. Chorin, “Numerical Solution of the Navier-Stokes Equations”, *Math. Comput.* **22**, 745 (1968).
- [23] H. Kopetsch, “Finite Differenz Verfahren für partielle Differentialgleichungen”, in *20. IFF Ferienkurs: Computersimulationen in der Physik* (KFA Jülich, Jülich 1989).
- [24] L. D. Landau and E. M. Lifshitz, *Hydrodynamik*, 3rd ed. (Akademie Verlag, Berlin, 1974).
- [25] J.-Z. Xue, E. Herbolzheimer, M. A. Rutgers, W. B. Russel, and P. M. Chaikin, “Diffusion, Dispersion and Settling of Hard Spheres,” *Phys. Rev. Lett.* **69**, 1715 (1992).
- [26] J. Martin, N. Rakotomalala, and D. Salin, “Hydrodynamic Dispersion Broadening of Sedimentation Front”, *Phys. Fluids Lett.* **6**, 3215 (1994).
- [27] G. K. Batchelor, “Sedimentation in a Dilute Polydisperse System of Interacting Spheres: 1. General Theory,” *J. Fluid Mech.* **119**, 379 (1982).
- [28] F. Feuillebois, D. Bruneau, R. Anthore, F. Feuillebois, X. Auvray, and C. Petipas, “Measurement of the average velocity of sedimentation in a dilute polydisperse suspension of spheres,” *J. Fluid Mech.* **221**, 577 (1990).
- [29] R. E. Caffish and J. H. C. Luke, “Variance in the sedimentation speed of a suspension,” *Phys. Fluids* **28**, 759 (1985).

## Figure Captions

**Figure 1:** Sedimentation of polydisperse spheres at  $\Phi = 0.157$ : **(a)** particle trajectories in the laboratory frame, **(b)** particle trajectories in the comoving frame of the sedimenting cloud. The particle coordinates have been shifted to start at a common origin and the coordinate change due to the mean settling velocity has been subtracted.

**Figure 2:** Dimensionless  $x$  ( $\bigcirc$ ) and  $y$  ( $\star$ ) mean square displacements [ $\langle x_*^2 \rangle \equiv \langle x^2 \rangle / \bar{r}^2$  and  $\langle y_*^2 \rangle \equiv \langle y^2 \rangle / \bar{r}^2$ ] as functions of dimensionless time  $t^* \equiv tV_S / \bar{r}$  averaged over four runs. The two solid lines indicate a linear approximation to the data in an intermediate time regime. The slope of these lines equals twice the dimensionless diffusion constants  $D_x^*$  and  $D_y^*$ .

**Figure 3:** **(a)** Dimensionless particle self-diffusion constants  $D_x^*$  ( $\star$ ) and  $D_y^*$  ( $\bigcirc$ ) as a function of solid fraction  $\Phi$ . We have displayed errorbars on selected data points to indicate deviations of the mean obtained from  $n$  averages over different initial configurations [ $\Phi = 0.16$ :  $n = 6$ ,  $\Phi = 0.31$ :  $n = 5$ , all other concentrations:  $n = 3$ ]. **(b)** Dimensionless ratio  $D_y/D_x$  of self-diffusivity parallel ( $D_y$ ) and perpendicular ( $D_x$ ) to settling direction ( $\bigcirc$ ) and the experimental data from Nicolai et al. [5] (+).

**Figure 4:** **(a)** Hindered settling function  $f(\Phi)$ . The graph corresponds to data with a fixed ratio of grid spacing to particle size  $\Delta x / \bar{r} = 2.5$  ( $\bigcirc$ ) and  $1.25$  ( $\star$ ) respectively. The solid curve is given by  $(1 - \Phi)^3$ . **(b)** To demonstrate the influence of grid spacing on the accuracy of our results, we display the hindered settling function for different solid fraction  $\Phi$  as a function of the ratio of grid spacing to average particle radius  $\Delta x / \bar{r}$ . From top to bottom the curves correspond to  $\Phi = 0.079$ ,  $0.16$ ,  $0.24$ ,  $0.31$  and  $0.39$  respectively.

**Figure 5:** **(a)** Dependence of the width of the velocity distribution  $\Delta v_y^*$  on the volume fraction. We show simulation data for a polydispersity of  $p = 0.04$  ( $\bigcirc$ ), measured data by Nicolai et al. for  $p \approx 0.04$  (+) and Xue et al. [25] for  $p = 0.01$  ( $\times$ ). In all cases, the fluctuations  $\Delta v_y^*$  and  $\Delta v_x^*$  have been made non-dimensional by division through the Stokes velocity. Errorbars on selected data points indicate the deviation of the mean for averages over different initial conditions, their number being equal to the numbers in Fig. 3a. **(b)** Ratio of  $\Delta v_y^*$  to  $\Delta v_x^*$ . We show simulated data at  $p = 0.04$  ( $\bigcirc$ ) and the experimental results of Nicolai et al. [5] (+).

|           |                               |                 |           |
|-----------|-------------------------------|-----------------|-----------|
| $L_x$     | system width                  | 3               | $cm$      |
| $L_y$     | system height                 | 6               | $cm$      |
| $\eta$    | liquid shear viscosity        | 0.192           | $g/cm\ s$ |
| $\rho_l$  | liquid density                | 1.09            | $g/cm^3$  |
| $z$       | Stokes force reference length | 0.06            | $cm$      |
| $\rho_p$  | particle density              | 2.53            | $g/cm^3$  |
| $\bar{r}$ | average particle radius       | 0.03            | $cm$      |
| $p$       | polydispersity                | 0.04            |           |
| $k_n$     | repulsion constant            | $1 \times 10^6$ | $g/s^2$   |
| $g$       | gravitational acceleration    | 980             | $cm/s^2$  |

Table 1: List of fixed simulation parameters. Unless otherwise specified, simulations runs have been performed using the parameters in this table.

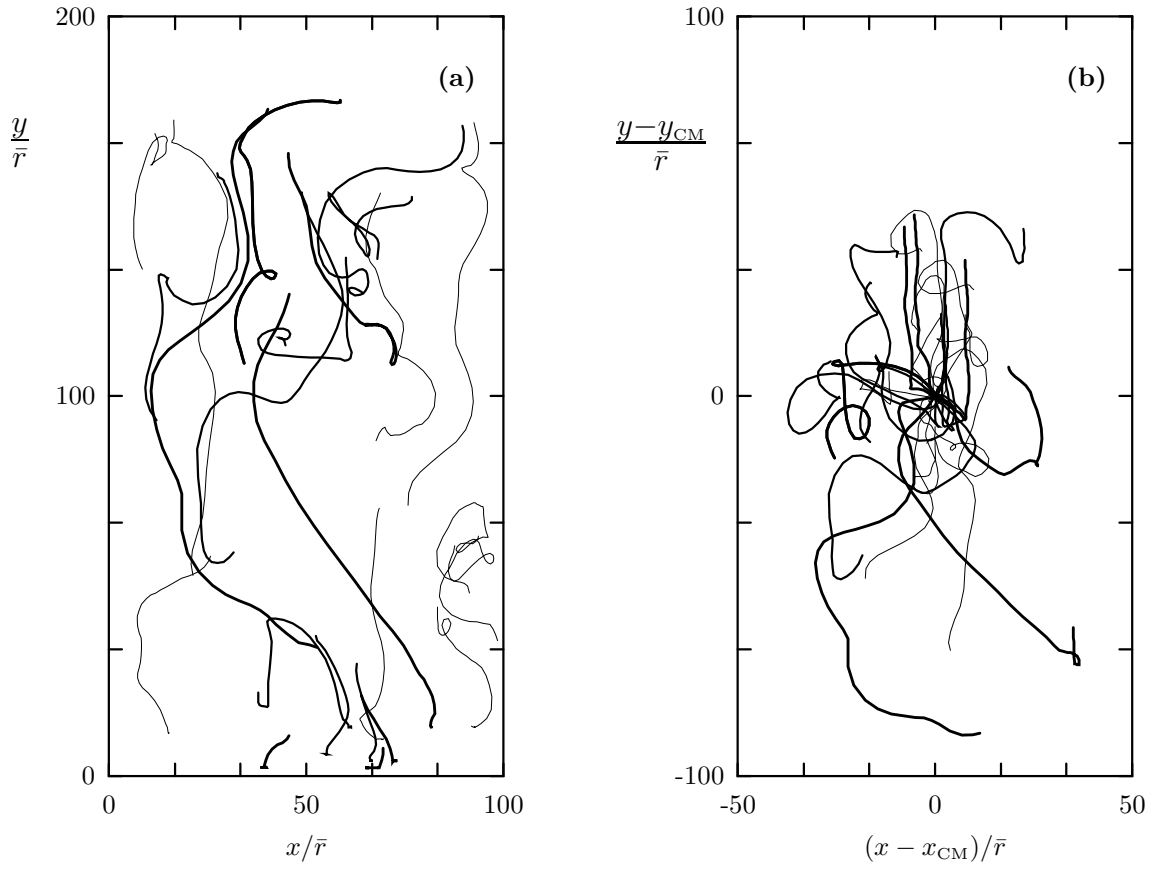


Figure 1:

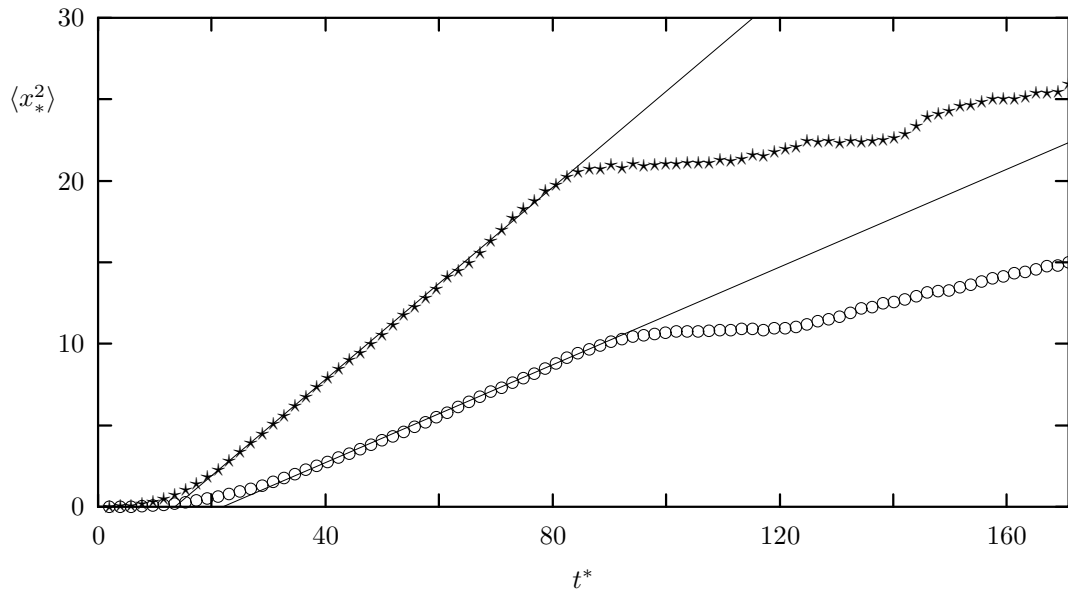


Figure 2:

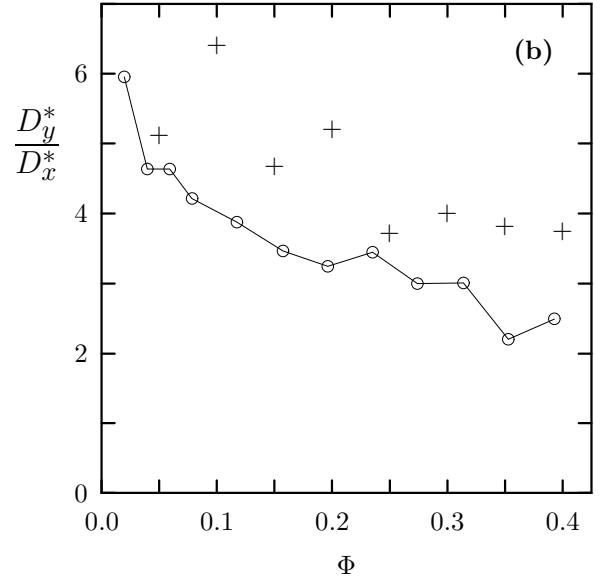
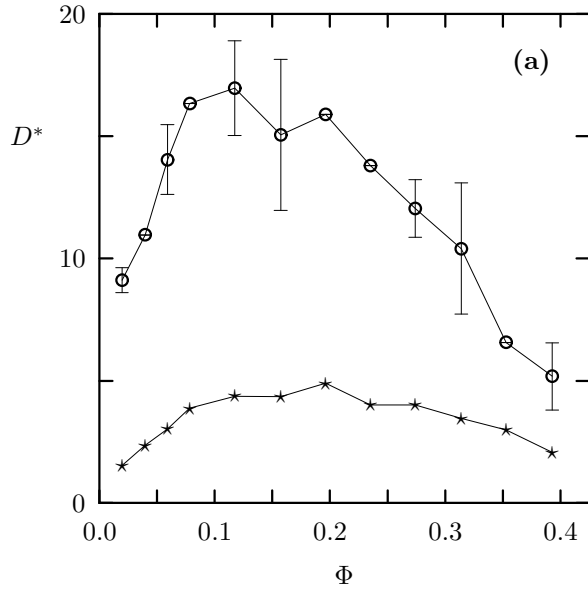


Figure 3:

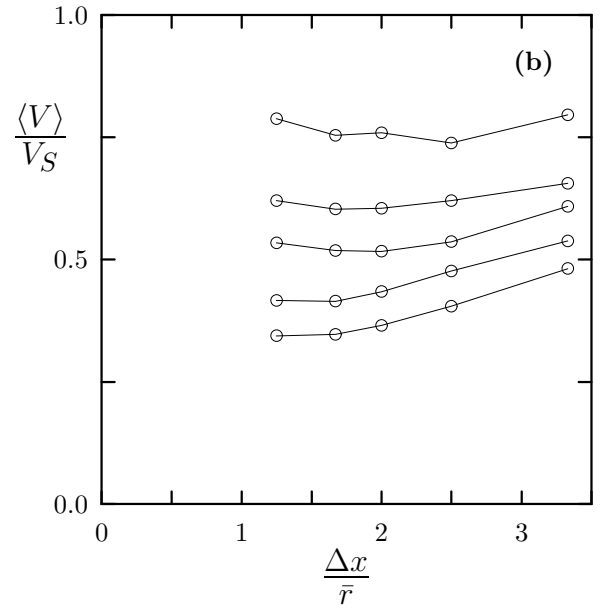
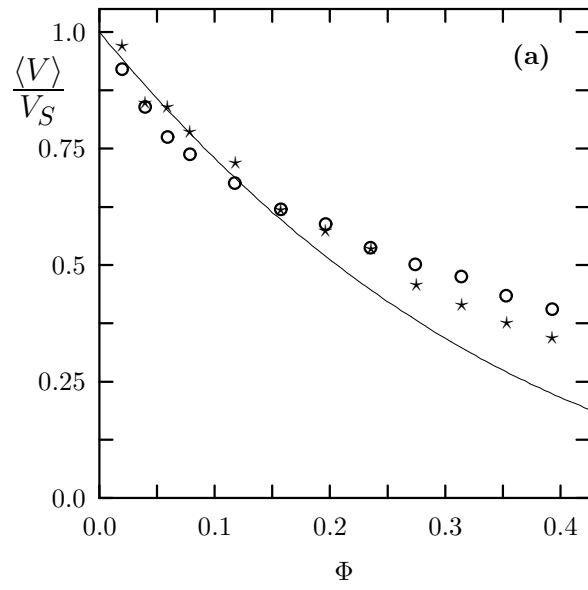


Figure 4:



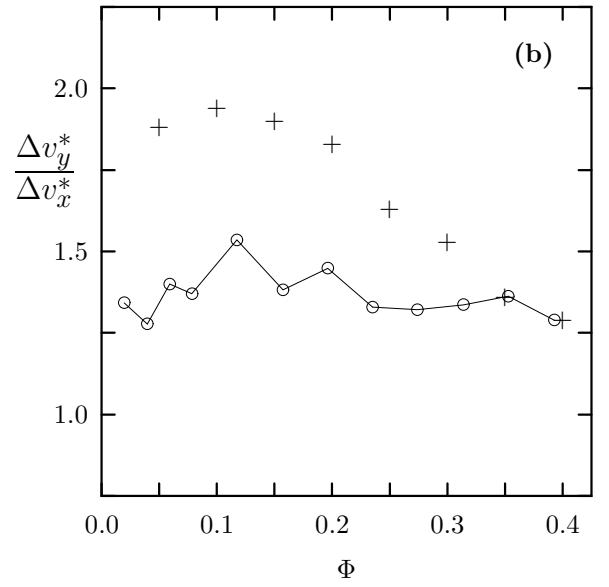
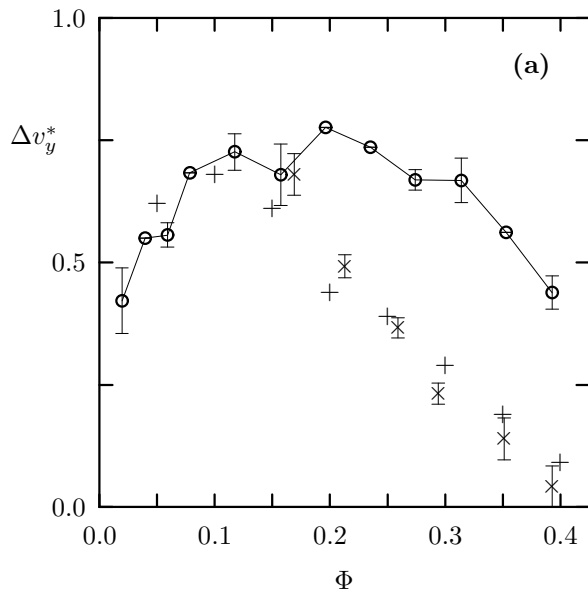


Figure 5: